Supplemental Materials: Correlated disorder induced anomalous transport in time reversal symmetry breaking topological insulator

Takuya Okugawa,[1] Tanay Nag,[1,*] and Dante M. Kennes[1,2,†]

[1] *Institut für Theorie der Statistischen Physik, RWTH Aachen, 52056 Aachen, Germany and JARA - Fundamentals of Future Information Technology.*
[2] *Max Planck Institute for the Structure and Dynamics of Matter, Center for Free Electron Laser Science, 22761 Hamburg, Germany.*

I. QSHI MODEL

In this section, we extensively discuss the QSHI model as given by the Eq. (1) of the main text. The model Hamiltonian for a QSHI is the following [1, 2]

$$H_0(\boldsymbol{k}) = \boldsymbol{N}\cdot\boldsymbol{\Gamma} = \sum_{i=1}^{3} N_i\Gamma_i \tag{1}$$

where $N_1 = v_F\sin(k_y a)/a$, $N_2 = -v_F\sin(k_x a)/a$, $N_3 = m(\boldsymbol{k}) = m_0 + 2B[2-\cos(k_x a)-\cos(k_y a)]/a^2$ and $\Gamma_1 = \tau_x\sigma_0$, $\Gamma_2 = \tau_y\sigma_z$, and $\Gamma_3 = \tau_z\sigma_0$. We note that $\boldsymbol{\tau}\in\{A,B\}$ and $\boldsymbol{\sigma}\in\{\uparrow,\downarrow\}$ represent orbital and spin degrees of freedom. Here, v_F (a) denotes the Fermi velocity (lattice spacing). The QSHI model in Eq. (1) supports gapless helical edge modes, protected by TRS $\mathcal{T} = i\tau_z\sigma_x\mathcal{K}$ with $\mathcal{K}$ being the complex conjugate operator: $\mathcal{T}H_0(\boldsymbol{k})\mathcal{T}^{-1} = H_0(-\boldsymbol{k})$. The model becomes trivially gapped for $m_0/B > 0$ (B is chosen to be positive). This model has unitary chiral symmetry and anti-unitary particle-hole symmetry, respectively, generated by $\mathcal{C} = \tau_y\sigma_x$ and $\mathcal{P} = \tau_x\sigma_z\mathcal{K}$: $\mathcal{C}H_0(\boldsymbol{k})\mathcal{C}^{-1} = -H_0(\boldsymbol{k})$ and $\mathcal{P}H_0(\boldsymbol{k})\mathcal{P}^{-1} = -H_0(-\boldsymbol{k})$. Interestingly, the QSHI model has mirror symmetry $M_{xy} = \mathcal{C}_4 M_y$: $M_{xy}H_0(k_x,k_y,k_z)(M_{xy})^{-1} = H_0(k_y,k_x,k_z)$ where $\mathcal{C}_4$ [M_y] represents the generator of the four-fold rotational symmetry [mirror symmetry along y-axis]. A magnetic field, breaking TRS, can be introduced in the model, as discussed in Eq. (2) of the main text: $H(\boldsymbol{k}) = H_0(\boldsymbol{k}) + gM\tau_z\sigma_z$ where g being the Lande-g factor and M is the magnetic exchange field. The chiral edge modes in $H(\boldsymbol{k})$ are preserved by the anti-unitary symmetry while the model does not have the unitary symmetry.

II. RESERVOIR EFFECT

In this section, we analyze Fig. 3 (e) of the main text where the QSCI phase is no longer observed although the upper and lower block Hamiltonian $H_{u,l}(\boldsymbol{k})$ both become topological with $\overline{m}_0^{u,l} < 0$ as predicted by SCBA for disorder strength $W > 550$ meV. Such a counter-intuitive observations can be caused by a reservoir effect that we explain below at length. In order to understand the underlying reason, we vary the topological mass term from m_0 to m_1 in the QSHI leads such that $|m_1| > |m_0|$ while keeping the Hamiltonian $H_{\rm CS}(m_0, M, W)$ of the central system unaltered (see Fig. 1).

We concentrate on longitudinal quasi-periodicity $\epsilon_i = W\cos(2\pi\eta i + \phi)/2$ with $\phi\in[0,2\pi)$ in the central system. At first, we consider a lead Hamiltonians given by $H_{L,R}(-|m_0|)$. Following the SCBA, the QSCI phase is expected to show up after the QAHI phase when increasing W. In the conductance G, we observe such a behavior for $gM = 30$ meV (see Fig. 1 (e)) while for strong magnetic field $gM = 52$ meV (see Fig. 1 (i)), there is no signature of the QSCI phase following the QAHI phase upon increasing W. We now change the lead Hamiltonians to $H_{L,R}(-|m_1|)$. In this case, we find the QAHI phase is followed by a QSCI phase for $gM = 30$, and 52 meV from the conductance analysis (see Figs. 1 (g) and (k)) which are in accordance with the SCBA. Therefore, enhancing the topological mass ($|m_1| > |m_0|$) in the QSHI leads could resolve the apparent existence of a trivial phase in conflict with $\overline{m}_0^{u,l} < 0$ from SCBA. Importantly, the robustness of the QSCI phase in Fig. 1 (g) is confirmed by $\delta G\to 0$ as shown in Fig. 1 (h). This is different from Fig. 1 (f) where δG does not completely vanish inside the QSCI phase.

In addition, the QAHI phase with $gM = 52$ meV is not accurately captured by the SCBA for $H_{L,R}(-|m_0|)$. We find a certain zone in the phase diagram with $G < 1$ inside the predicted QAHI phase as shown by the red patches. This zone is bounded by the solid blue and purple dashed lines of SCBA, for $gM = 52$ meV (see Fig. 1 (i)). These non-quantized patches vanish when the QSHI leads are given by $H_{L,R}(-|m_1|)$ instead of $H_{L,R}(-|m_0|)$ complying with the SCBA for the above choice of the leads (see Fig. 1 (k)).

Note that when a topological mass term of higher magnitude is considered for the QSHI leads i.e., $|m_1| > |m_0|$, the effects of the reservoir gets suppressed. This effect may arise once the topological gap of the lead is less than or comparable to the gap of the central system. The interface between central system and leads essentially causes the bulk modes of the leads to hybridize with the edge modes of the central system resulting in the contamination of the topological properties for the latter [3]. Hence, only by increasing the mass term in the QSHI leads, we recover the quantized edge transport

* tnag@physik.rwth-aachen.de
† dkennes@physik.rwth-aachen.de

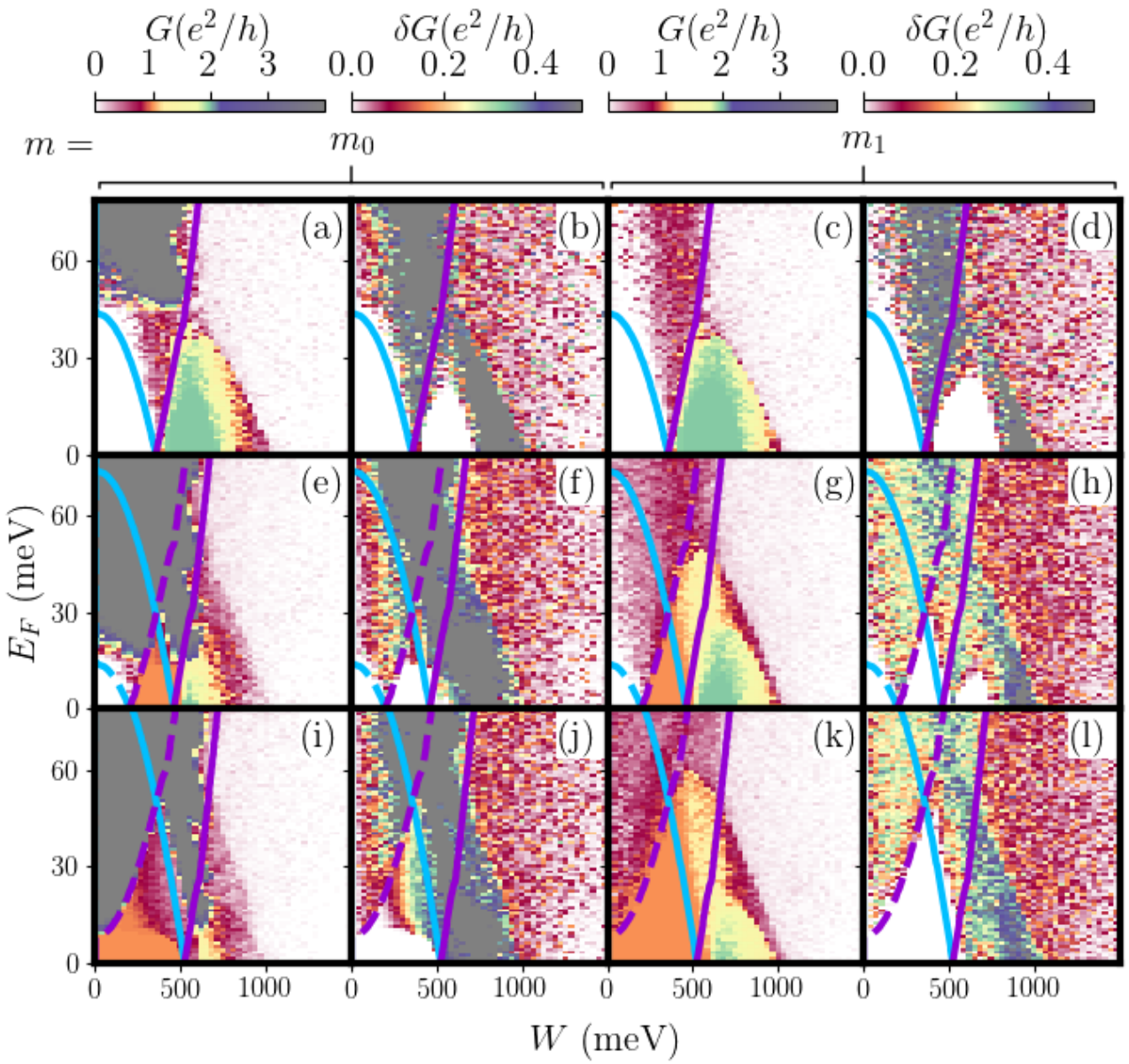

FIG. 1. (color online) (a), (e), and (i) [(c), (g), and (k)] depict the conductance G with $gM = 0$, 30 and 52 meV, respectively, for the longitudinal quasi-periodicity $\epsilon_i = W\cos(2\pi\eta i + \phi)/2$, considering the QSHI lead Hamiltonian $H_{L,R}(-|m_0|)$ ($m_0 = 44$ meV) [$H_{L,R}(-|m_1|)$ ($m_1 = 80$ meV)]. The corresponding standard deviation δG are shown for the longitudinal quasi-periodicity with $H_{L,R}(-|m_0|)$ [$H_{L,R}(-|m_1|)$] in (b), (f), and (j) [(d), (h), and (l)]. The system sizes are taken to be $L_x = 400a$ for all panels and $L_y = 100a$ for (a)-(d) and $L_y = 200a$ for (e)-(l). Notice that the central system is always described by the Hamiltonian $H_{\rm CS}(m_0, M, W)$ irrespective of the topological mass term in the leads. The QSCI phase does [does not] appears for $gM = 52$ meV after QAHI phase for (k) [(i)] referring to the fact that the topological mass term in the QSHI leads is responsible for such phenomena.

of the central system more accurately. Upon inspecting the phase diagrams in Fig. 1, one can comment that the topological gap in the leads $|m_1|$ has to be much larger than the renormalized bulk gap Δ of the central system ($|m_1| \gg |\Delta|$) to prevent bulk states of the leads from hybridizing with the edge modes in the central system.

III. PHASE DIAGRAMS AND BAND STRUCTURES

Here, we discuss how one can understand the phase diagram for transverse quasi-periodicity which is shown in Fig. 4 of the main text, from the band structure of the isolated central system considering $L_x \to \infty$. In this case k_x can be considered as a good quantum number due to

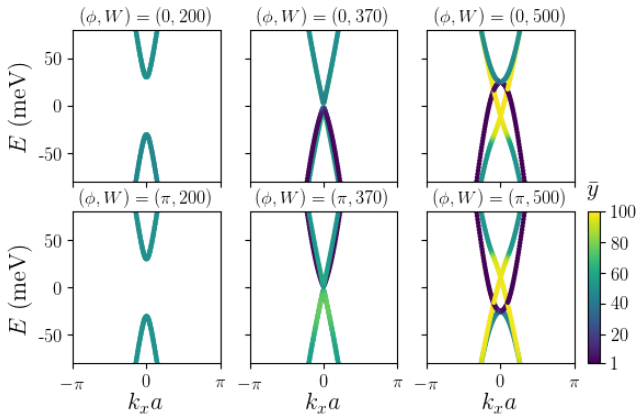

FIG. 2. (Color online) The energy dispersion of the non-magnetic isolated central system (Eq. (2) of the main text) in presence of transverse quasi-periodic potential ($\alpha = 0$ and $\beta = 1$) under the stripe geometry with infinite (open) boundary condition along x (y)-direction. Here, we depict the TPT between the NI $\rightarrow$ QSHI phase i.e., $G = 0 \rightarrow G = 2$, as shown in Fig. 4 (a) of the main text. We can find the $G = 0$ phase for $W = 200$, the TPT at $W = 370$ and the $G = 2$ phase for $W = 500$. Moreover, we separately consider $\phi = 0$ and π to emphasize the emergent symmetry $E(k_x, W) = -E(-k_x, -W)$. The colorbar denotes the average localization $\overline{y}$ of a given momentum mode at k_x in the finite y-direction.

the translation symmetry along the x-direction. Notice that the quasi-periodic potential along the y-direction breaks the translation symmetry only along that direction. This enables us to probe the band structures by varying the disorder strength i.e., the amplitude of quasi-periodic potential W. The results are shown in Figs. 2, 3 and 4, respectively, for $gM = 0$, 30 and 52 meV.

We numerically diagonalize $H_{\rm CS}(m_0, M, W) = \sum_{j,j',k_x}[\mathcal{H}_{j,j',k_x}(m_0, M) + \epsilon_j \delta_{j,j'}]C^\dagger_{j,k_x} C_{j',k_x}$ considering $\epsilon_j = W\cos(2\pi\eta j + \phi)/2$ and $j = 1, \cdots, L_y$ with $C = \{C_{A\uparrow}, C_{A\downarrow}, C_{B\uparrow}, C_{B\downarrow}\}$. Here, $\mathcal{H}_{j,j',k_x}(m_0, M)$ is obtained after the partial inverse Fourier transformation of $H(\boldsymbol{k})$ in Eq. (2) of the main text along the y-direction only. We further simplify the situation by considering only two specific values of $\phi = 0$ and π such that $\epsilon_j \rightarrow -\epsilon_j$ or equivalently $W \rightarrow -W$ for $\phi \rightarrow \phi + \pi$. This allows us to look for the correlation between the energy dispersion and sign reversal in W in a concrete manner. In addition, we measure average localization of each momentum mode in the y-direction, associated with eigenenergy $E_n(k_x)$, as follows $\bar{y}_n(k_x) = \sum_{j=1}^{L_y} j(\sum_q |\psi_{n,q}(j, k_x)|^2)$ where $\psi_{n,q}(j, k_x)$ is the j-th component of n-th eigenstate in the basis $q = \{A\uparrow, A\downarrow, B\uparrow, B\downarrow\}$ as obtained from $H_{\rm CS}(m_0, M, W)$ (see the colorbars in Fig. 2, 3 and 4).

For the non-magnetic case as demonstrated in Fig. 2, we find that TPTs between the NI and QSHI phase are found for $(\phi, W) = (0, 370)$ and $(\pi, 370)$ (W in units of meV). Here the gap between the doubly degenerate bulk valence and conduction bands vanishes while the trivial [topological] gap is observed for $(\phi, W) = (0, 200)$ and $(\pi, 200)$ [$(\phi, W) = (0, 500)$ and $(\pi, 500)$]. In the topological case with $W = 500$, we find helical edge modes inside the bulk gap $-25 < E < 25$ (in the units of meV) for $\phi = 0$ and π while there exist no edge mode within the trivial gap for $W = 200$. Notice that the critical disorder strength $W_c \approx 360$, separating the QSHI from the NI phases, (see Fig. 4 (a) of the main text), can be approximately traced by the systematic investigations on the band structure in a stripe geometry with $L_x \rightarrow \infty$ considered here.

In the same spirit, for magnetic field $gM = 30$ meV, the TPTs between NI and QAHI phase occur at $W_{c,1} = 200$ and $W_{c,2} = 500$ for the TPTs separating QAHI from QSCI phase (see Fig. 3). The size of the trivial and topological gap, respectively, for the disorder amplitudes $W = 100$, and 300, 400, 600 are consistent with Fig. 4 (b) in the main text. The important point to note here is that the QAHI (QSCI) phase hosts one (two) pair(s) of chiral mode(s) due to TRS breaking. In the present case, the QAHI (QSCI) phase supports chiral modes coming from the lower block Hamiltonian (both the lower and upper block Hamiltonian). We repeat the same analysis for $gM = 52$ meV in Fig. 4 where the TPT between the QAHI and QSCI phase takes place at $W_c = 580$. The trivial (topological) gap hosting no (edge) modes are depicted for $W = 400$ ($W = 700$). Two pairs of chiral edge modes can also be seen inside the topological gap for the QSCI phase.

One also notes that $E(k_x) \rightarrow -E(-k_x)$ for $\phi \rightarrow \phi + \pi$. Together with $W \rightarrow -W$ for $\phi \rightarrow \phi + \pi$, we can obtain an equivalence, $E(k_x, W) = -E(-k_x, -W)$. This gives rise to the symmetric nature of the phase diagrams under phase averaging in the main text for $\pm E_F$. Hence, we only restrict ourselves to positive values of E_F while investigating the phase diagrams in Figs. 2, 3 and 4 of the main text.

IV. NORMALIZED PARTICIPATION RATIO

We now study the normalized participation ratio (NPR) I_n from the eigenvectors of a system with the spatial dimension $L_x \times L_y$, defined by

$$I_n = \left\langle \left(\sum_{i=1}^{pL_xL_y} |\psi_n(i)|^4 \right)^{-1} \right\rangle / (pL_xL_y). \qquad (2)$$

Here the eigenvector for a given energy level E_n is denoted by ψ_n. In the present case, we consider the isolated disordered central system $H_{\rm CS}(m_0, M, W) = \sum_{rr'}[\mathcal{H}_{rr'}(m_0, M) + \epsilon_r \delta_{r,r'}]C^\dagger_r C_{r'}$ where $\mathcal{H}_{rr'}(m_0, M)$ is obtained after inverse Fourier transformation of $H(\boldsymbol{k})$ as given in Eq. (2) of the main text. The $\langle ... \rangle$ in Eq. (2) hence indicates the disorder average and $p = 4$ as we have 2 orbital and 2 spin degrees of freedom. For the uniformly delocalized eigenvectors in 2D, ψ_n extends equally over

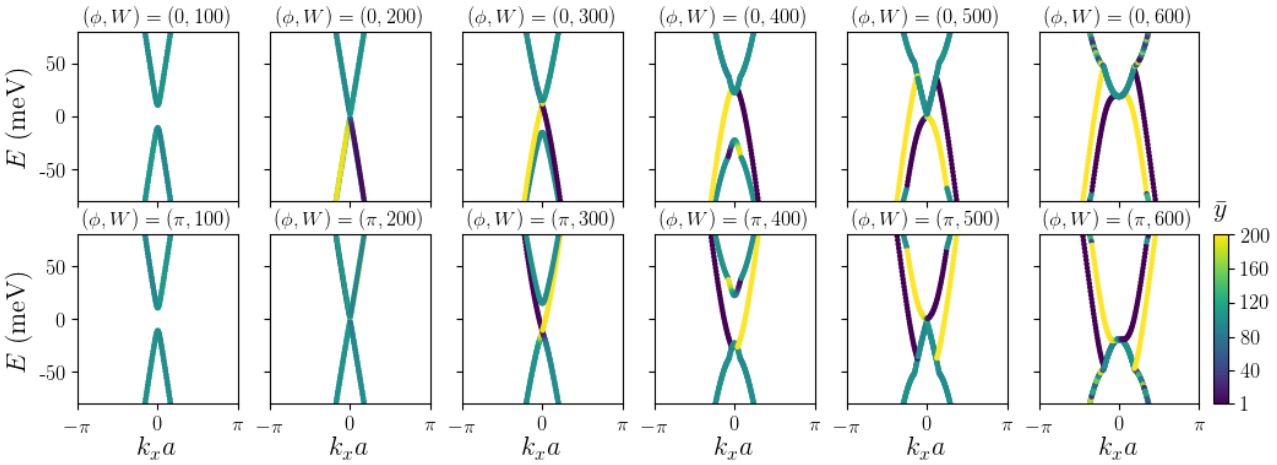

FIG. 3. (Color online) The energy dispersion of the isolated central system (Eq. (2) of the main text) for $gM = 30$ meV in presence of transverse quasi-periodic potential ($\alpha = 0$ and $\beta = 1$) under the stripe geometry with infinite (open) boundary condition along x (y)-direction. Here, we depict TPTs between the NI $\rightarrow$ QAHI phase i.e., $G = 0 \rightarrow G = 1$, the QAHI $\rightarrow$ QSCI phase i.e., $G = 1 \rightarrow G = 2$, as shown in Fig. 4 (c) of the main text. We can find a $G = 0$ phase for $W = 100$, the TPT between NI and QAHI at $W = 200$, $G = 1$ phase for $W = 300$ and $W = 400$, the TPT between QAHI and QSCI phase at $W = 500$, $G = 2$ QSCI phase for $W = 600$. Moreover, we separately consider $\phi = 0$ and π to emphasize the emergent symmetry $E(k_x, W) = -E(-k_x, -W)$. The color bar denotes the average localization of a given momentum mode at k_x in the finite y-direction.

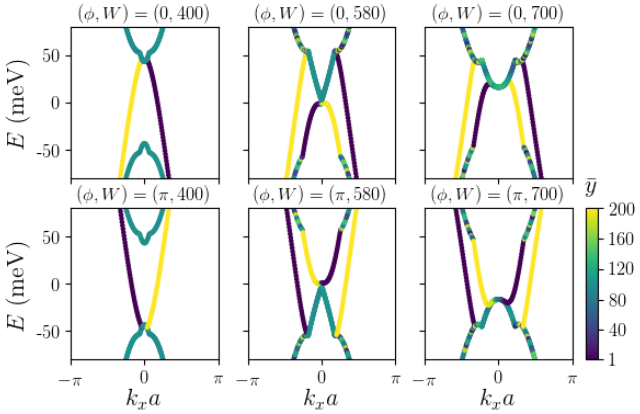

FIG. 4. (Color online) The energy dispersion of the isolated central system (Eq. (2) of the main text) for $gM = 52$ meV in presence of transverse quasi-periodic potential ($\alpha = 0$ and $\beta = 1$) under the stripe geometry with infinite (open) boundary condition along x (y)-direction. Here,we depict TPT between the QAHI $\rightarrow$ QSCI phase i.e., $G = 1 \rightarrow G = 2$, as shown in Fig. 4 (e) of the main text. We can find a $G = 1$ phase for $W = 400$, the TPT between $G = 1$ and $G = 2$ at $W = 580$ and $G = 2$ phase for $W = 700$. Moreover, we separately consider $\phi = 0$ and π to emphasize the emergent symmetry $E(k_x, W) = -E(-k_x, -W)$.

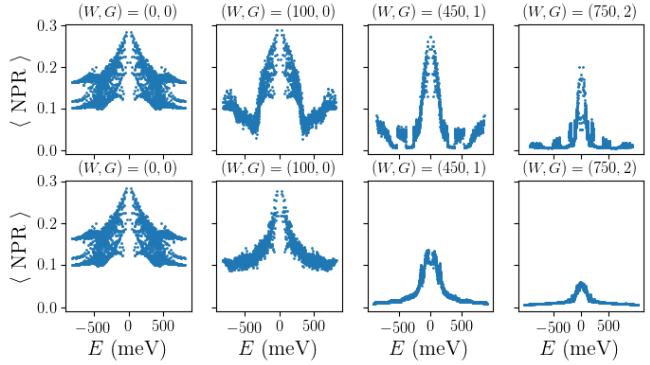

FIG. 5. (Color online) We illustrate the average NPR I_n, following Eq. (2) for the isolated central system of dimension 30×30, with isotropic and anisotropic longitudinal quasi-periodicities in upper and lower panel, respectively. The energy window of mobility edge shrinks for the longitudinal case as compared to the isotropic case under substantially strong disorder. We consider $gM = 30$ meV and (W, G) are stated accordingly.

all sites $|\psi_n(i)|^2 \sim (pL_xL_y)^{-1}$. The NPR I_n thus approaches unity for the uniformly delocalized state. For a localized state with the localization length ε, one obtains the $|\psi_n(i)|^2 \sim \varepsilon^{-1}$. Hence, NPR becomes vanishingly small when $\varepsilon \ll \sqrt{L_xL_y}$. We compute the disorder averaged energy $\langle E_n \rangle$ and study the NPR profile as a function of $\langle E_n \rangle$ depicted in Fig. 5 upper and lower panel for isotropic and longitudinal quasi-periodicity, respectively, with $gM = 30$ meV fixed. For 1D systems, the NPR turns out to be very important to probe the mobility edge profile, demarcating the localized states from the delocalized states, in the single particle spectrum [4–7].

For the 2D case, one can similarly define an energy interval $E_- < E < E_+$ within which the NPR takes higher

value for the extended modes. We start with the clean case $(W, G) = (0, 0)$ where a mobility edge is absent (see Fig. 5). Upon increases W we observe that the delocalized states are symmetrically located around zero energy (bounded within $E_\pm$ i.e., around the centre of the spectrum) and localized states are found to appear away from zero energy (outside the $E_\pm$ i.e., around the edge of the spectrum). This refers to the emergence of mobility edge for the disordered 2D system. Note that within our analysis, limited by finite size, multiple mobility edges might occur (see Fig. 5 $(W, G) = (450, 1)$ upper panel). The signature of extended modes becomes more pronounced for some intermediate disorder window (see upper and lower panels in Fig. 5 $(W, G) = (100, 0)$, $(450, 1)$). The energy window associated with the mobility edge is smaller for the anisotropic case compared to the isotropic case for intermediate disorder strength.

Interestingly, we find quantized transport but with $G > 2$ stemming from extended bulk modes for the isotropic quasi-periodicity as shown in Fig. 2 of main text. This is the same scenario where a mobility edge is promoted. Therefore, the low energy extended bulk states within the mobility edge might be responsible for the quantized transport for the isotropic case when E_F lies outside of the bulk gap Δ of the central system. For the anisotropic quasi-periodicity in contrast, the mobility edge shrinks more rapidly with W as compared to the isotropic case. Therefore, low energy extended bulk modes might not appear when E_F is outside of the bulk gap Δ.

V. SCBA BASED ON THE CONTINUUM MODEL

In this section, we present the SCBA analysis based on the continuum model, derived from the Eq. (2) in the main text. The self-energy Σ, as formulated by a 2×2 matrix is given by $(E_F - H - \Sigma)^{-1} = \langle (E_F - \mathcal{H})^{-1} \rangle$ where $\langle \cdots \rangle$ represents the disorder average and H ($\mathcal{H}$) denotes the 2×2 $\boldsymbol{k}$ space (disordered real space) Hamiltonian. We expand the Eq. (2) of the main text around the $\boldsymbol{\Gamma} = (0, 0)$ point to write down the Hamiltonian

$$H(\boldsymbol{k}) = \begin{pmatrix} H_u(\boldsymbol{k}) & 0 \\ 0 & H_l(\boldsymbol{k}) \end{pmatrix}, \text{ with } H_{l,u}(\boldsymbol{k}) = \begin{pmatrix} a_{l,u} & b_{l,u} \\ c_{l,u} & d_{l,u} \end{pmatrix} \tag{3}$$

where $a_{l,u} = m_0 + Bk^2 \mp gM$, $b_{l,u} = v_F(k_y \mp ik_x)$, $c_{l,u} = b^*_{l,u}$ and $d_{l,u} = -a_{l,u}$. The inverse block Hamiltonian $[H_{l,u}(\boldsymbol{k})]^{-1}$ thus takes the form

$$[H_{l,u}(\boldsymbol{k})]^{-1} = \frac{1}{a_{l,u}d_{l,u} - b_{l,u}c_{l,u}} \begin{pmatrix} d_{l,u} & -b_{l,u} \\ -c_{l,u} & a_{l,u} \end{pmatrix}, \tag{4}$$

The Fourier transformation of the disorder correlation function $C_{m,n} = \langle \epsilon_{i,j}\epsilon_{i+m,j+n} \rangle = W^2 \cos\left[2\pi\eta(m\alpha + n\beta)\right]/8$ is given by

$$\begin{aligned} C(\boldsymbol{k}) &= \frac{W^2}{8} \sum_{\boldsymbol{R}} e^{i\boldsymbol{k}\cdot\boldsymbol{R}} \cos\left[2\pi\eta(m\alpha + n\beta)\right] \\ &= \frac{W^2}{16} \left[\delta_{k_x a,\alpha Q}\delta_{k_y a,\beta Q} + \delta_{k_x a,-\alpha Q}\delta_{k_y a,-\beta Q}\right] \end{aligned} \tag{5}$$

with $Q = 2\pi\eta$ and $\boldsymbol{R} = a(m\alpha, n\beta)$, where $m(n) \in [1, L_x/a(L_y/a)]$.

The self energy, using Eq. (3) of the main text by setting $\Sigma_{l,u} = 0$ in the right hand side, is thus given by [8–10]

$$\begin{aligned} \Sigma_{l,u} &= \frac{W^2}{16} \left[\frac{1}{M^+_{l,u}} + \frac{1}{M^-_{l,u}}\right] \\ &= \sum_{k_x = Q^\pm_x, k_y = Q^\pm_y} \begin{pmatrix} A_{l,u}(k_x, k_y) & B_{l,u}(k_x, k_y) \\ C_{l,u}(k_x, k_y) & D_{l,u}(k_x, k_y) \end{pmatrix}. \end{aligned} \tag{6}$$

We note that the self-energy for the correlated case is thus characteristically different from that of the random disorder where the correlation function $C(\boldsymbol{k})$ no longer depends on $\boldsymbol{k}$. Due to the structure of the correlation function $C(\boldsymbol{k})$ here, the $\boldsymbol{k}$-sum reduces to a δ-function. Here $M^\pm_{l,u} = E_F + i\zeta - H_{l,u}(\pm\alpha Q, \pm\beta Q)$. We denote $Q^\pm_x = \pm\alpha Q$ and $Q^\pm_y = \pm\beta Q$. One can obtain

$$[A, D]_{l,u} = \left(\frac{W^2}{16}\right) \frac{1}{\tilde{a}_{l,u}\tilde{d}_{l,u} - \tilde{b}_{l,u}\tilde{c}_{l,u}} [\tilde{d}, \tilde{a}]_{l,u} \tag{7}$$

where $\tilde{a}$'s are function of k_x and k_y with $\tilde{a}_{l,u} = E_F + i\zeta - a_{l,u}$, $\tilde{d}_{l,u} = E_F + i\zeta + a_{l,u}$, $\tilde{b}_{l,u} = -b_{l,u}$ and $\tilde{c}_{l,u} = -b^*_{l,u}$. The complete expressions of $[A, D]_{l,u}$ are found to be

$$\begin{aligned} A_{l,u} &= \frac{W^2}{16} \sum_{k_x,k_y} \frac{E_F + i\zeta + (m_0 + Bk^2 \mp gM)}{(E_F + i\zeta)^2 - (m_0 + Bk^2 \mp gM)^2 - v_F^2 k^2} \\ D_{l,u} &= \frac{W^2}{16} \sum_{k_x,k_y} \frac{E_F + i\zeta - (m_0 + Bk^2 \mp gM)}{(E_F + i\zeta)^2 - (m_0 + Bk^2 \mp gM)^2 - v_F^2 k^2}. \end{aligned} \tag{8}$$

Here subscripts l, u in the left hand side correspond to $\mp$ sign in the right hand side.

We are interested in the computation of $\Sigma^{l,u}_0 = (A_{l,u} + D_{l,u})/2$ and $\Sigma^{l,u}_z = (A_{l,u} - D_{l,u})/2$ that yield the renormalized mass $\overline{m}^{l,u}_0 = m_0 + \delta m_{l,u}$ and chemical potential $\overline{E}^{l,u}_F = E_F + \delta\mu_{l,u}$ as given by

$$\begin{aligned} \delta\mu_{l,u} &= -\mathrm{Re}[\Sigma^{l,u}_0] \\ &= -\left(\frac{W^2}{8}\right) \frac{E_F}{E_F^2 - v_F^2 x - (m_0 + Bx \mp gM)^2} \\ \delta m_{l,u} &= \mathrm{Re}[\Sigma^{l,u}_z] \\ &= \left(\frac{W^2}{8}\right) \frac{m_0 + Bx \mp gM}{E_F^2 - v_F^2 x - (m_0 + Bx \mp gM)^2} \end{aligned}$$

with $x = Q^2(\alpha^2 + \beta^2)$. The TAI phase is supported in the presence of disorder for $\overline{m}_0^{l,u} < 0$. The correction in the mass term $\delta m_{l,u}$ turns out to be negative when $m_0 + Bx \mp gM < 0$ $[m_0 + Bx \mp gM > 0]$ for $E_F^2 - v_F^2 x - (m_0 + Bx \mp gM)^2 > 0$ $[E_F^2 - v_F^2 x - (m_0 + Bx \mp gM)^2 < 0]$. The analytical findings hint to the situation when both $\delta m_l < 0$ and $\delta m_u < 0$ for different combinations of numerator and denominator. Since $\delta m_{l,u} < 0$ can be satisfied regardless of the sign of E_F referring to the fact that TAI phases can exist for positive and negative values of E_F.

VI. TOPOLOGICAL PHASE TRANSITIONS PREDICTED BY SCBA BASED ON THE LATTICE MODEL

We now address the SCBA analysis (Eq. (3) of the main text), based on the lattice Hamiltonian, that accurately complies with the Landauer-Büttiker numerical results. Examining Figs. 2, 3, and 4 of the main text, we below discuss the phase boundaries following the profiles of $\overline{m}_0^{l,u}$ and $|\overline{E}_F^{l,u}|$. The TPTs, separating QAHI from the trivial phase, are captured when $\overline{m}_0^l$ reverses its sign simultaneously with $|\overline{E}_F^l| = \pm\overline{m}_0^l$. The QAHI phase is found to be bounded by dashed purple and solid blue in all figures. The QAHI thus appear when $\overline{m}_0^l < |\overline{E}_F^l| < -\overline{m}_0^l$ and $\overline{m}_0^u > 0$. Similarly, the TPTs between QAHI and QSCI phases, marked by the coincidence of solid blue and purple lines, are associated with sign changes in $\overline{m}_0^u$ (while $\overline{m}_0^l < 0$) simultaneously with $|\overline{E}_F^u| = \pm\overline{m}_0^u = 0$. The QSCI/ QSHI phase appears on the right side of the solid purple line. However, the boundary between the QSCI/QSHI and AI phases can not be captured by SCBA. Following the same line of argument, the QSCI/ QSHI phase is expected to be confined within $\overline{m}_0^{u,l} < |\overline{E}_F^{u,l}| < -\overline{m}_0^{u,l}$ and $\overline{m}_0^{u,l} < 0$.

[1] B. A. Bernevig, T. L. Hughes, and S.-C. Zhang, Science **314**, 1757 (2006).
[2] J. Wang, B. Lian, and S.-C. Zhang, Phys. Rev. Lett. **115**, 036805 (2015).
[3] T. Okugawa, P. Tang, A. Rubio, and D. M. Kennes, Phys. Rev. B **102**, 201405 (2020).
[4] J. Biddle, D. J. Priour, B. Wang, and S. Das Sarma, Phys. Rev. B **83**, 075105 (2011).
[5] R. Modak and S. Mukerjee, Phys. Rev. Lett. **115**, 230401 (2015).
[6] R. Modak and T. Nag, Phys. Rev. Research **2**, 012074 (2020).
[7] X. Deng, S. Ray, S. Sinha, G. V. Shlyapnikov, and L. Santos, Phys. Rev. Lett. **123**, 025301 (2019).
[8] R. Zimmermann and C. Schindler, Phys. Rev. B **80**, 144202 (2009).
[9] A. Girschik, F. Libisch, and S. Rotter, Phys. Rev. B **88**, 014201 (2013).
[10] Y. Fu, J. H. Wilson, and J. H. Pixley, Phys. Rev. B **104**, L041106 (2021).